Proceedings of the Robert A. Welch Foundation 40th Conference on Chemical Research: Chemistry on the Nanometer Scale (The Robert A. Welch Foundation, Houston, 1997); pp.165-187.

CHAPTER-11

ONE-DIMENSIONAL NANOSTRUCTURES: RATIONAL SYNTHESIS, NOVEL PROPERTIES AND APPLICATIONS*

CHARLES M. LIEBER, Alfredo M. Morales, Paul E. Sheehan, Eric W. Wong, and Peidong Yang, Department of Chemistry and Chemical Biology, Harvard University, Cambridge, Massachusetts

Introduction

Nanometer scale structures are currently the focus of considerable interest since they represent ideal systems for testing fundamental ideas about the roles of dimensionality and confinement in materials, and represent potential building blocks for nanostructured materials, composites and novel electronic devices of greatly reduced size.[1-3] To address and impact in a significant way these interesting problems necessarily requires interdisciplinary approaches that integrate, for example, the development of methods to synthesize rationally nanostructures of varying composition, dimensionality and size, and measurements of the physical properties of these materials. From the standpoint of one-dimensional (1D) structures, there has been significant interest and speculation about the properties and potential applications of carbon nanotubes and nanotubes filled with other materials.[4-7] While carbon nanotubes can now be produced in relatively pure form,[8] approaches used to prepare filled nanotubes[5-7] have not yet led to the preparation of significant quantities of pure materials that are needed to test the possibly unique properties of these highly anisotropic materials. Clearly, there exist both opportunity and need to develop synthetic approaches to prepare these and other 1D systems in pure form. Furthermore, the rational design of any device will require a fundamental understanding of the properties of these materials and how they depend on, for example, dimensionality and size. For instance, the electrical and mechanical properties of carbon nanotubes have generated considerable interest and speculation,[9-14] although direct measurements of the intrinsic resistivity and mechanical strength of individual nanotubes has been difficult. This situation reflects the general difficulty in attaching connections from the outside world to nanometer scale objects,

---

* Based on an address presented by Charles M. Lieber before "The Robert A. Welch Foundation 40th Conference on Chemical Research, Chemistry on the Nanometer Scale," which was held in Houston, Texas, October 21-22, 1996.

and thus suggests that the development of new technologies that probe the properties of single nanostructures could impact significantly this emerging area of chemistry.

In this review, an overview of our work addressing several critical issues in chemistry at the nanometer scale will be addressed with a particular emphasis on 1D nanometer scale structures. First, synthetic strategies that can be exploited to prepare successfully 1D nanostructures of a variety of different classes of materials, including carbides, elemental semiconductors and oxides, will be discussed. Next, new methods that we have developed to characterize the physical properties of individual nanostructures will be described. Examples of unique electrical and mechanical properties exhibited by carbon nanotubes and carbide nanorods are discussed. Lastly, we explore the organization of 1D nanostructures into a bulk, composite materials. Nanostructured high-temperature superconductors have been prepared using magnesium oxide nanorods. The introduction of 1D nanorods into the superconductor matrix has led to significant enhancements in the current carrying capabilities of these materials. Furthermore, studies of the detailed structure of these nanorod-superconductor composites have led to the formulation of a general scheme of self-organization as a means for creating rationally nanostructured materials.

Synthesis of 1-Dimensional Nanostructures

There are several general approaches that can be considered when developing syntheses for 1D nanostructures. First, it is possible to prepare the material on or within a preexisting template of the desired size and shape of the final product; that is, template mediated growth.[15-17] In addition, there are two scenarios by which a controlled nucleation step can be used to prepare a 1D structure. In one, a catalyst is chosen that form a liquid alloy with the desired crystalline phase.[18] This liquid alloy will be the preferred site of vapor deposition, and when supersaturated, serves as a point of crystal growth. This catalyst-based mechanism is termed vapor-liquid-solid (VLS) when gas phase reactants are utilized in the growth. In the second, 1D structures are prepared through a vapor-solid (VS) growth mechanism. Both the VLS and VS mechanisms have been exploited in the past to produce 1-100 μm diameter structures termed whiskers.[18-20] As will be shown below, it is also possible to produce 1D nanostructures using VLS and VS approaches when the nucleation step is carefully controlled. Regardless of the synthetic approach pursued, it is important to recognize that the final products must be formed in relatively pure and ideally single-crystal form to be useful in, for example, fundamental studies of physical properties or applications. The examples presented below meet these requirements.

We have recently demonstrated that a range of chemically distinct 1D carbide nanostructures, termed carbide nanorods, can be prepared in relatively pure and crystalline form via the reaction of carbon nanotubes with volatile transition metal and main group oxide or halide species (Figure 1).[15-17]

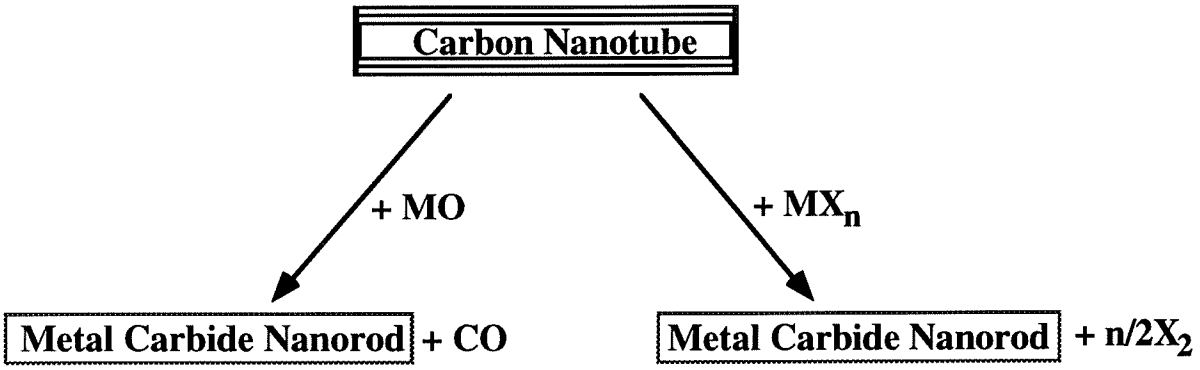

FIGURE 1

Schematic diagram of the reactions used to prepare carbide nanorods. MO corresponds to a volatile metal or main group oxide and MX_n corresponds to a volatile metal or main group halide complex.

Previous studies have also shown that SiO vapor can be used to covert carbon fibers[21] and nanotubes[22] to SiC rods, although the sizes of these SiC products are typically much larger than the carbon precursor.[22] In our studies discussed below, the diameters of the solid nanorods are similar to the starting diameters of the nanotube reactants and significantly smaller than reported in these previous structures. Furthermore, our general approach (Figure 1) has been exploited to prepare a wide range of chemically distinct carbide materials, including SiC.

A typical example of a reaction between a volatile metal oxide and carbon nanotubes is that involving TiO. The morphology and structure of the nanorod products obtained from the reaction of TiO with carbon nanotubes at 1375°C have been characterized by transmission electron microscopy (TEM), electron diffraction and X-ray diffraction. Typical TEM images of two different rods are shown in Figure 2. These images show that the reaction products exhibit straight and smoothly curved, solid rod-like structures that are distinct from the irregularly curved and hollow carbon nanotube reactant. In addition, these images show that rods can grow with smooth surfaces or exhibit regular faceting that we have termed a saw-tooth structure.[15] The

diameters of the rod-like products are similar to that of the carbon nanotubes, 2-30 nm, and the lengths typically exceed 1 μm. Energy dispersive X-ray fluorescence and electron energy loss spectroscopy measurements have further shown that these nanorods contain only titanium and sp^3-hybridized carbon as expected for TiC.

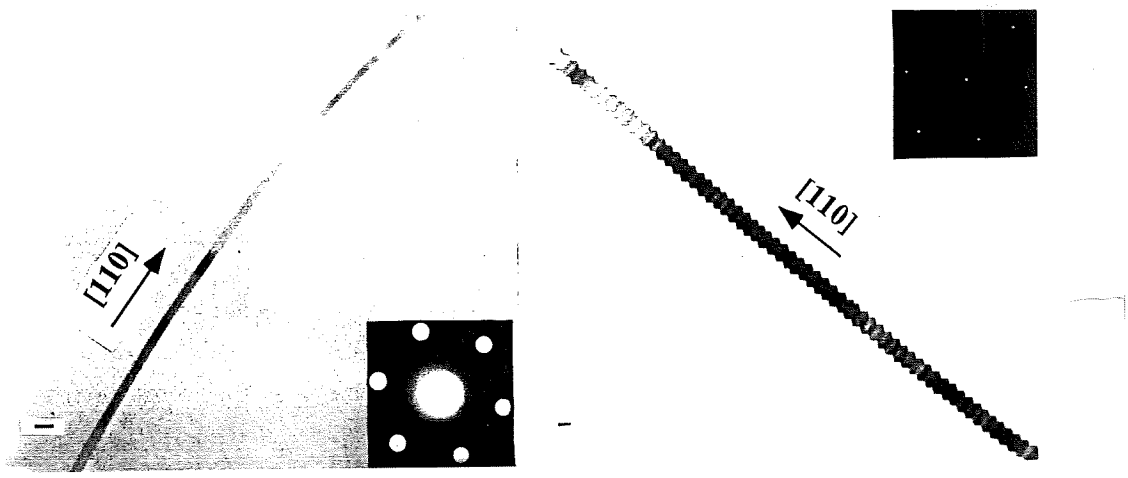

FIGURE 2

TEM images of TiC nanorods. The scale bars correspond to 20 nm. The insets correspond to electron diffraction patterns recorded along <111> zone axes that are perpendicular to the axes of the two nanorods.

The TiC nanorods have also been characterized by X-ray and electron diffraction measurements. Powder X-ray diffraction data from samples produced using TiO exhibit diffraction peaks that can be indexed to the known rock salt structure of TiC with no evidence of either graphitic (nanotube), Ti-metal or Ti-oxide peaks present. The TiC nanorods also appear to be single crystals with a very low density of stacking faults. Convergent beam electron diffraction patterns recorded along the <111> zone axis perpendicular to the axis of the smooth nanorod (Figure 2) exhibit a lattice constant and six-fold symmetry corresponding to the (111) planes of cubic TiC. These data imply that the axis of the smooth TiC nanorods is [110]. Similar studies of the saw-tooth nanorod (Figure 2) demonstrate that the rod axis is also [110] for this morphology as well. The [110] direction is not unique for the TiC nanorods since we have also observed [111] growth direction in several individual rods.

Our approach (Figure 1) to carbide nanorod synthesis appears to be general. For example, structural and composition analyses of the material produced from the reaction of carbon nanotubes with Si and I_2 are consistent with the formation of silicon carbide (SiC)

nanorods. TEM images show that the SiC nanorods produced from this reaction are relatively straight, solid rods. The diameters of the SiC rods produced in the Si + I_2 reaction at 1200°C are typically 2-20 nm (similar to the diameters of the carbon nanotube reactants), and have lengths on the order of 1 μm. These diameters are significantly smaller than reported recently for the reaction of SiO with impure nanotubes at 1700°C.[22] TEM data also show that these SiC nanorods possess a high density of planar defects in contrast to the near single crystal TiC nanorods. We have suggested[15] that the defects in [111] oriented rods are rotational twin stacking faults in analogy to previous observations made on larger SiC wiskers.[19]

Results from the synthesis of other metal carbides using our approach are summarized in Table-1.

Material	Reactant (temp., °C)	Structure	Properties
TiC	TiO (1300-1400) Ti + I_2 (1200-1300)	single crystal	metal
NbC	Nb + I_2 (≥700)	polycrystalline	superconductor
Fe_3C	$FeCl_3$ (1350)	amorphous	ferromagnetic
SiC	Si + I_2 (1100-1200) SiO (1300-1450)	single crystal	semiconductor
BC_x	B_2O_2 (1400)	polycrystalline	insulator

TABLE 1

Summary of the structure and properties of carbide nanorods prepared by reaction of volatile oxide and halide species with carbon nanotubes.

For example, the reaction of Nb-metal and I_2 with carbon nanotubes yields NbC nanorods. XRD shows that this reaction results in the complete conversion of the nanotubes into the cubic, rock salt phase of NbC. TEM images and selected area electron diffraction show that the NbC nanorods produced in these reactions are polycrystalline with morphologies similar to the carbon nanotube starting materials.[15-17] Significantly, these polycrystalline nanorods are also found to be superconducting like bulk NbC. While exhaustive studies of the growth of all known carbide materials have not been carried out, the data summarized in Table-1 highlight the generality of

this template approach to carbide-based nanorods. Because the metal and main group carbides exhibit interesting properties, ranging from conducting TiC and NbC to superstrong SiC, these nanorods offer exciting opportunities for both fundamental research and technological applications. Mechanical measurements made on individual carbide nanorods are discussed below.

We have also explored the catalytic VLS mechanism as an approach to preparing 1D nanostructures. As an example of this work is the first synthesis of bulk silicon nanowires.[23] The synthesis of 1D silicon is especially interesting since as the diameter of a silicon wire is reduced it is predicted to become a direct band gap semiconductor, and thus an efficient light emitter.[24] This may well explain luminescence in porous silicon, although the ill-defined structure of this latter material has precluded unambiguous identification of the origin of light emission.

Our studies of the growth of silicon nanowires were carried out using a high pressure, high-temperature laser ablation system (Figure 3). Briefly, targets containing silicon and iron

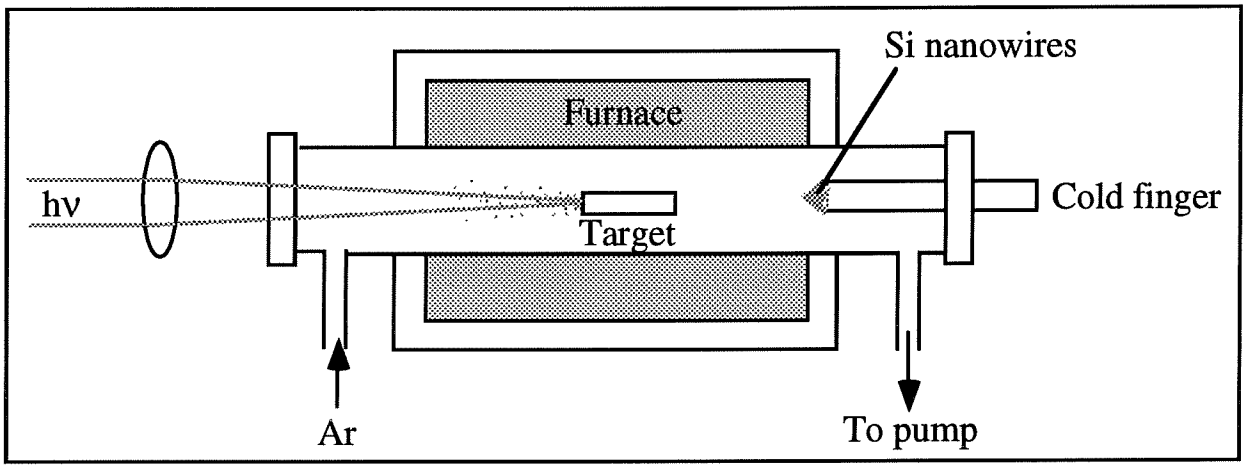

FIGURE 3

Schematic diagram of the apparatus used to synthesize 1D silicon nanowires.

were ablated under argon with a frequency doubled Nd:YAG laser in a heated tube furnace. The ablated material was deposited on a water cooled copper cold finger placed at the end of the heated zone. Ablation of $Si_{0.9}Fe_{0.1}$ targets at 1150-1200°C yielded silicon nanowires 10 to 30 nm in diameter and up to 30 μm in length. The composition and structure of these nanowires were determined by transmission electron microscopy (TEM) and energy dispersive x-ray fluorescence (EDX) as shown in Figure 4.

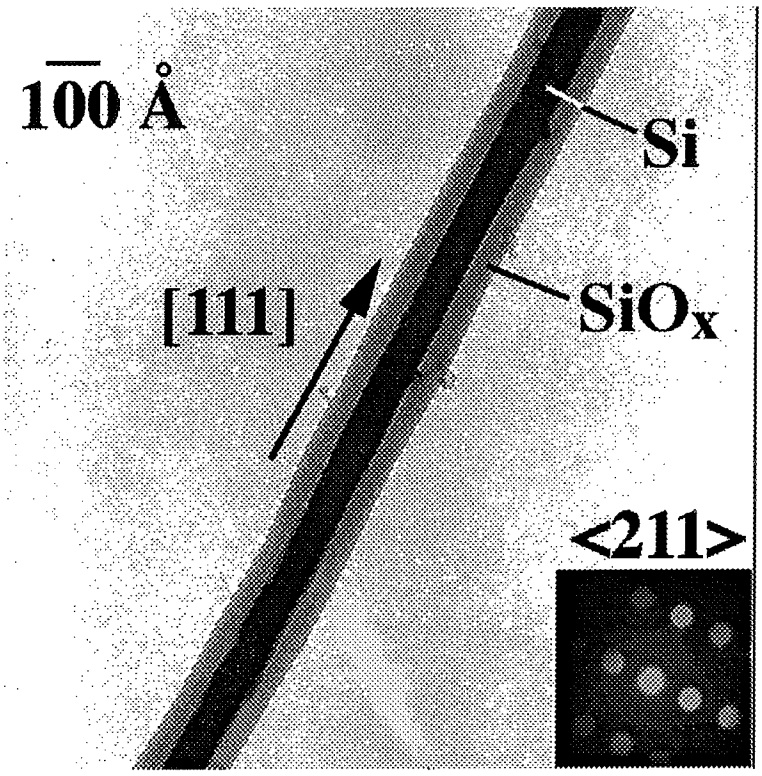

FIGURE 4

TEM image of a single Si nanowire produced by the laser ablation technique. The inset shows electron diffraction pattern recorded along the <211> zone axis.

The TEM images (e.g., Figure 4) show that the nanowires possess a crystalline silicon core and an amorphous SiO_x coating. Electron diffraction patterns recorded along the <211> zone axis of the silicon lattice indicate that growth direction of the nanowires is along [111]. Atomic resolution TEM micrographs confirm that the (111) atomic planes (separation 0.31 nm) are perpendicular to the growth direction and thus that nanowire growth axis is [111].

Images of these nanowires have also shown that nearly spherical particles terminate the ends of almost every wire (Figure 5). Composition and structure analyses of these terminating spheres show that they are crystalline $FeSi_2$. The observation of these metal silicide particles suggest strongly that $FeSi_2$ functions as a catalyst in the VLS growth of the Si nanowires. That $FeSi_2$ functions as a catalyst in the growth process is supported strongly by temperature dependent growth studies and the know Fe-Si phase diagram.[23] In short, the growth process

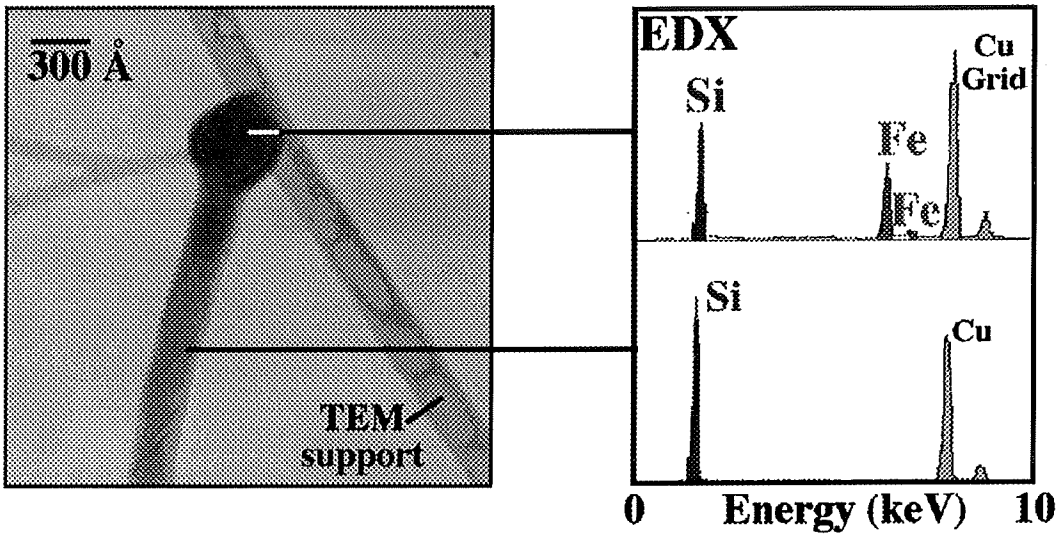

FIGURE 5

TEM image (left) of the end of s single Si nanowire. EDX composition map (right) of the two distinct regions of the nanowire.

involves (1) generation of atomic Si and Fe species by laser ablation, (2) cooling and clustering to form $FeSi_x$ liquid droplets, (3) growth of solid Si nanowires as the liquid droplets become supersaturated with excess Si and (4) growth termination as the temperature drops below ~1200 °C and the $FeSi_2$ solidifies. It is also important to note that a critical aspect of the successful growth of nanoscale wires is the generation of nanometer diameter catalyst particles. The laser ablation technique is particularly well-suited for this key task since the particle density and cooling/clustering rates can be readily varied through the experimental conditions. We have confirmed this general mechanistic scenario through silicon nanowire growth using Ni and Au metal catalysts that were chosen after examining the metal-silicon binary phase diagrams.

Lastly, we have also exploited the VS growth mechanism to synthesize MgO nanorods.[25] In this approach, Mg vapor is generated *in-situ* through carbothermal reduction of MgO, and then transported in a flow reactor to a growth zone where nucleation and reoxidation to MgO occurs. The critical nucleation step determining the growth of MgO rods with nanometer-scale diameters can be reproducibly controlled using MgO nanoclusters 5 to 8 nm in diameter or by chemical etching of MgO (100) single crystal surfaces. Low-magnification TEM images show that the MgO nanorods are straight or gently curved and range in diameter from 5 to 50 nm with a mean

of ~20 nm; the lengths typically exceed 2 μm (Figure 6). High-resolution imaging and electron diffraction measurements made on individual nanorods show that these

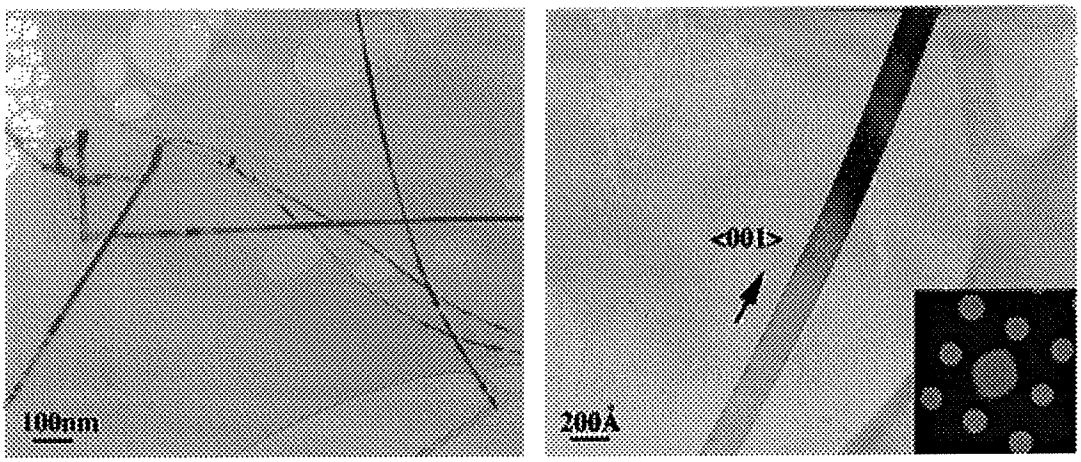

FIGURE 6

TEM images of MgO nanorods produced in bulk form using nanocluster nucleation sites. The <001> growth direction (right) was determined from convergent beam electron diffraction measurements (inset) taken perpendicular to the nanorod axis.

materials are single crystal, cubic MgO with a [001] rod axis (Figure 6). Interestingly, we have also been able to use this same synthetic approach to grow MgO nanorods on etched MgO single crystals surfaces as shown in Figure 7. Scanning electron microscopy (SEM) imaging shows that a high density of oriented MgO nanorods can be produced on planar substrates. The principle growth direction of the nanorods is normal to the substrate surface leading to a dense forest of rods with average diameters of 20 to 30 nm. The density of nanorods normal to the substrate surface in Figure 7 is ~$3x10^9/cm^2$, although higher and lower densities can be achieved through variations in the initial substrate etching conditions. TEM analysis of individual nanorods removed from the substrate surface demonstrate that the rods have the same single crystal structure and growth habit as the nanorods shown above in Figure 6.

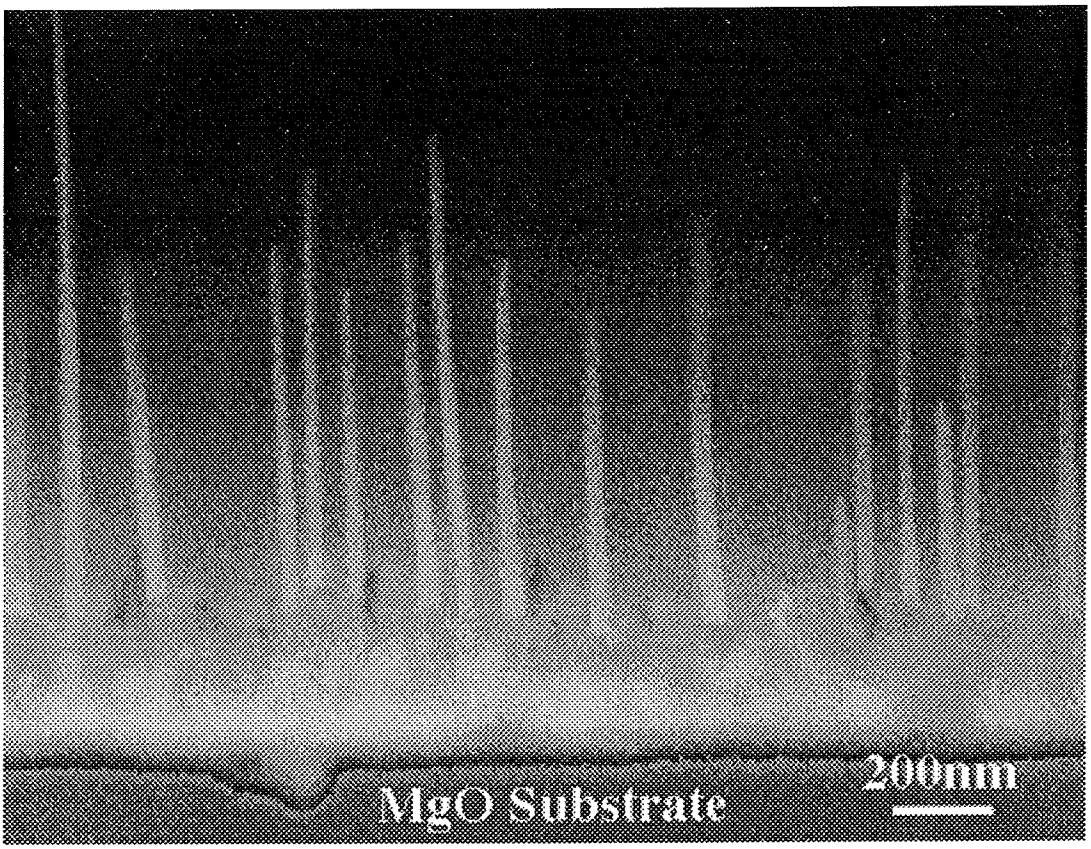

FIGURE 7

Forest of MgO nanorods grown perpendicular to the surface of a MgO single crystal.

Physical Properties of Nanorods and Nanotubes

The synthetic studies described above have expanded significantly the availability of 1D nanomaterials, and thus offer great opportunity to study how size and dimensionality affect physical properties. At the outset of this work, however, we were in the position of having many potentially interesting materials but no methods to probe their properties on an individual basis. Below we describe two new techniques, which exploit probe microscopy, that now enable the electrical and mechanical properties of individual nanostructures to be probed.

The approach used to measure the electrical properties of individual nanostructures is outlined in Figure 8.[26] For example, a drop of a nanotube suspension is deposited on a flat insulating surface and covered with a uniform layer of gold. To expose nanotubes for our measurements, a pattern of open slots is produced in the gold layer by conventional lithography procedures. Force microscopy studies have shown that this procedure yields many single nanotubes with one end covered by the gold pattern and the other end extending into the open

slots. By using a conducting cantilever-tip assembly in the force microscope, it is possible to contact electrically and measure the axial conduction through a single nanotube to the gold

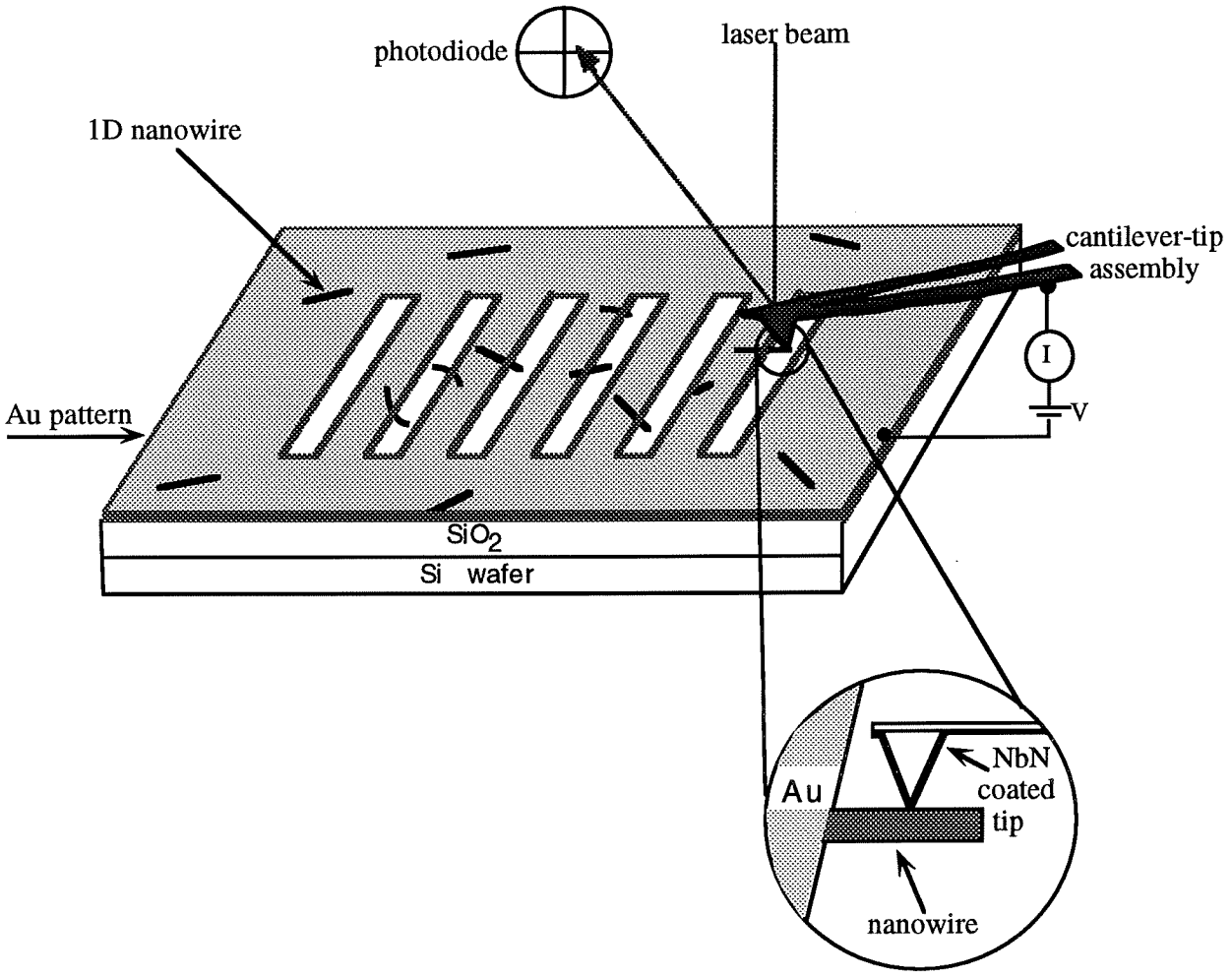

FIGURE 8

Schematic diagram illustrating the approach used to measure the electrical properties of individual 1D nanowires. Because the conductivity/resistance is measured at many points along a given structure, the technique is multiprobe (typically ≥100 points) and the contact resistance can be easily subtracted from the total signal.

contact while simultaneously recording the nanotube structure. Conducting tips were made by depositing NbN onto commercial Si_3N_4 cantilevers. This coating was chosen because it exhibits a combination of good conductivity and hardness. Soft conducting coatings like Au were insufficiently stable to provide reproducible measurements, and heavily-doped Si tips, while

robust, had excessively large contact resistances to the nanotube samples. It should be stressed that this technique is a multiprobe measurement since the resistance or conductivity is measured at many points along each nanotube or nanowire structure. In a typical experiment, this amounts to 100-500 separate spatial measurements, and thus it is quite trivial to subtract the contact resistance, which arise from the nanowire-gold and nanowire-tip junctions, from our signal. Our probe microscopy approach is thus similar to a conventional 4-probe resistivity measurements, except that we subtract contact resistance from our raw data versus pushing a "zero button" on a voltmeter. Additionally, we have the added advantage of being able to characterize the structure simultaneously with the resistance measurement.

In our studies, we can rapidly identify and focus on individual 1D nanowires by exploiting the high-resolution imaging capabilities of the force microscope. This point is illustrated clearly in images of the topography and resistance for a single carbon nanotube (Figure 9); this nanotube is connected to the gold overlayer slightly beyond the upper left of

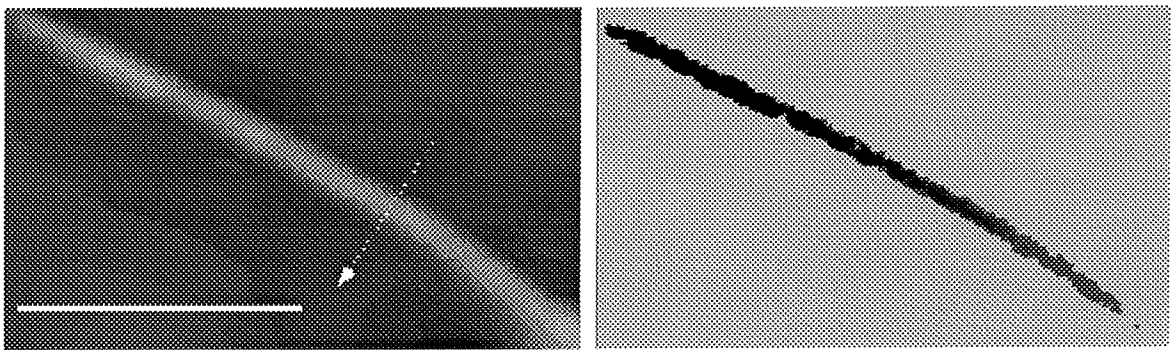

Figure 9

Topograph (left) and resistance (right) maps of a single, multiwall nanotube acquired simultaneously using the method outlined in Figure 8. The white scale bar corresponds to 0.5 μm. The arrow indicates the location of a cross-section used to determine the nanotube diameter.

the image. A cross section perpendicular to the axis of the nanotube shows that the height of the nanotube is 13.9 nm, and represents a good measure of the nanotube diameter.[26] The resistance image of the nanotube shows a monotonic resistance increase from the upper left (near to where it is connected to the gold electrode) to the lower right where it ends. A resistance plot taken along the nanotube axis of Figure 9 increases linearly with distance from the gold contact. The total resistance, R_T, in this and other measurements can be expressed as $R_T = R_C + R_S \cdot x$, where

the intercept R_c corresponds to the contact resistance in our measurement (the sum of gold-nanotube and nanotube-tip contact resistances), the slope R_S to the nanotube linear resistance and x to the position along the nanotube. Along the straight portion of this 13.9 nm diameter nanotube we observed a linear resistance of $R_S = 0.06$ Mohm/μm.

To compare the electrical properties of different nanotubes independent of their size we have calculated their resistivities (in microohm-meters) using the annular cross-sectional area (A_{cross}) of each sample, where $A_{cross} = \pi(r_{outer}^2 - r_{inner}^2)$ and r_{outer} and r_{inner} correspond to the outer and inner radii of the hollow nanotubes.[26] A summary of results obtained on single nanotubes with different diameters and structural defects are give in Table-2.

Sample	Diameter (nm)	Linear resistance (Mohm/μm)	Resistivity (μohm·m)	Structure
1	8.5	0.41	19.5 ± 2.0	straight
2	13.9	0.06	7.8 ± 1.0	straight
3	12.4	0.44	46.0 ± 1.8	slowly curved over ~1 μm length $\theta_1 \approx +5°$ $\theta_2 \approx -6°$ $\theta_3 \approx +7°$
4	15.0	0.25	37.6 ± 1.0	slowly curved over ~1 μm length $\theta \approx 17°$
5	18.5	0.22	48.9 ± 4.3	moderately curved over 1μm length $\theta \approx 30°$
6	9.5	1.93	117 ± 19	greatly curved over ~1 μm length $\theta_1 \approx +80°$ $\theta_2 \approx -65°$ $\theta_3 \approx +65°$

TABLE 2

Summary of carbon nanotube electrical resistivities.

These data highlight several important points. First, straight nanotubes without obvious structural defects exhibit the lowest resistivities. Among these samples, the resistivity decreases with

increasing diameter. The smallest resistivity that we have observed at room temperature, 7.8 μΩ-m, is still, however, nearly an order of magnitude greater than observed in single crystal graphite.

Structural defects also cause systematic increases in the nanotube resistivities. Comparison of samples with significant curvature (that is, samples 4 and 6) show clearly that the resistivity increases almost an order magnitude when compared to straight nanotubes of similar diameter (that is, samples 2 and 1, respectively). We believe that this comparison demonstrates clearly the importance of studying individual nanotubes that are structurally characterized to determine their intrinsic properties. It is also interesting to consider if by introducing defects directly with the probe tip or bending the nanotubes with the probe that it will be possible to probe the effects of electron scattering and bond strain in these one-dimensional structures.

The sensitivity of resistivity to structural imperfections must be accounted for to determine ultimately the intrinsic conductivity of nanotubes, but may also serve as a means to tailoring the resistance of these materials for applications such as strain sensors. We believe that our experimental approach provides a clear pathway to understanding nanotube electrical transport and to testing theoretical predictions, although this will require careful studies of the temperature and diameter dependencies of the resistivity for structurally characterized samples. The approach outlined here is also applicable to probing the intrinsic electrical properties of other 1D nanowires such as the carbide nanorods and silicon nanowires described above.

In addition, we have recently developed a related approach to probe the mechanical properties of 1D nanostructures.[27] To determine directly the mechanical properties of a rodlike structure requires that two connections be made to the material. One of these can be fixed but the other connection must enable displacement and force measurement. Here we use the same basic approach described above for electrical measurements: nanorods or nanotubes are dispersed randomly on the surface of a flat substrate, pinned to the substrate by depositing a regular array of square pads, and then the AFM is used to measure the lateral force necessary to deflect the structure at varying distances from the pinning point (Figure 10). To effectively pin the nanorods or nanotubes to this surface, we use pads of a rigid oxide that are deposited through a shadow mask. After depositing the oxide pinning pads, we use AFM to locate and characterize the lengths and diameters of protruding rods or tubes. A representative image of a pinned, 16 nm diameter carbon nanotube (Figure 10) shows that the our approach is readily achieved experimentally.

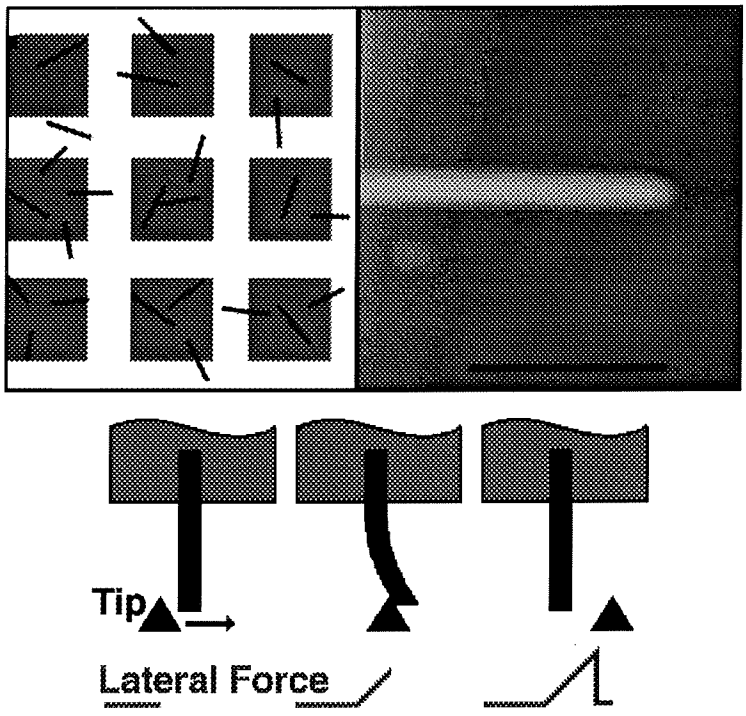

FIGURE 10

Schematic illustrating an array of square pads pinning randomly dispersed 1D nanostructures (upper left), an AFM topograph of a pinned carbon nanotube protruding from a single pad (upper right), and the expected lateral forces curves when the probe is used to deflect the 1D nanostructure (bottom).

Lateral force-displacement curves are recorded at different positions along the length of the nanorod or nanotube, as the tip is scanned perpendicular to the axis of the beam. After contact, the measured lateral force increases linearly as the beam is elastically deflected from its equilibrium position; the AFM tip remains on the surface during this deflection process. With continued bending it is possible to fracture or plastically deform a nanobeam and thereby determine its strength. Alternatively, the tip can move over the deflected structure if the beam restoring force exceeds a critical value determined by the applied normal load and cantilever spring constant.[28]

A typical plot of the lateral force versus displacement data recorded on an 11.5 nm diameter SiC nanorod is shown in Figure 11. This force-distance data were recorded while rastering the tip left to right (sample frame of reference). These data illustrate several important

points. First, the initial location at which the lateral force begins to increase in each horizontal scan is approximately the same. This shows that in each scan the nanorod returns to the same

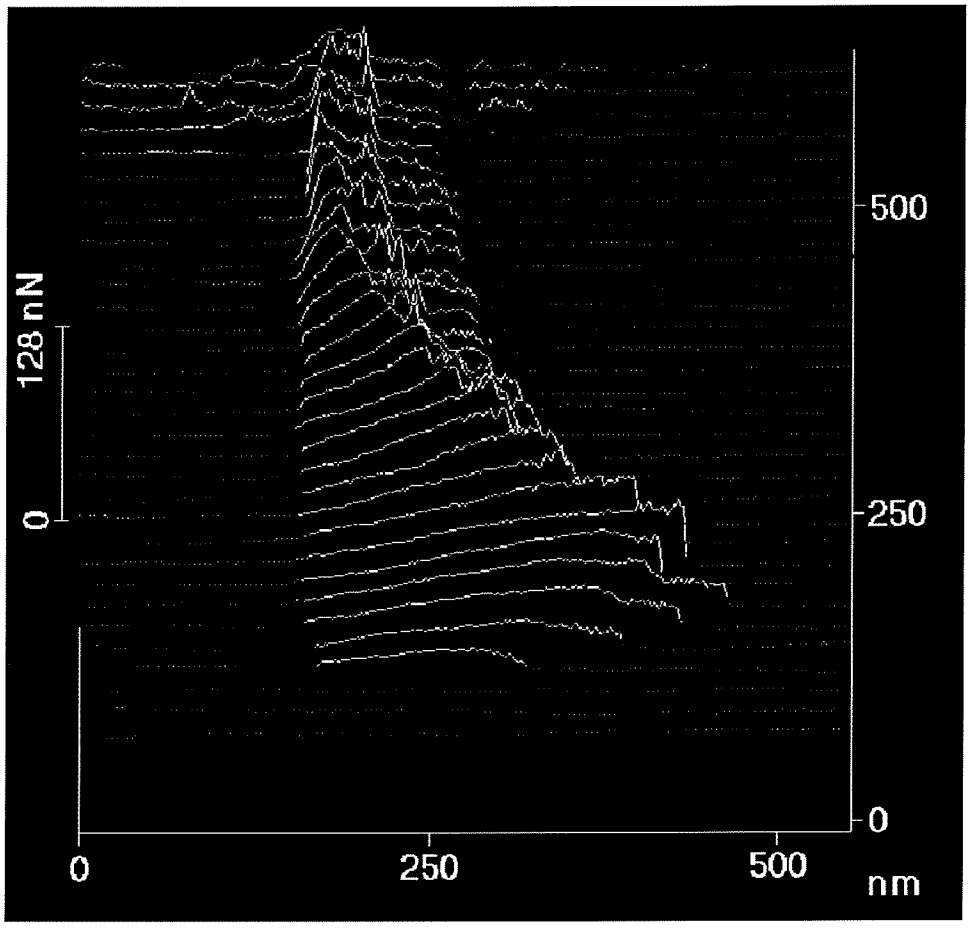

FIGURE 11
Force displacement data recorded on an 11.5 nm diameter SiC nanorod.

equilibrium position after the tip moves over the rod, and thus suggests that the beam deflection is elastic and that the nanorod-surface friction force is small compared to the beam restoring force. Second, the lateral force recorded in each of the individual scans increases linearly once the tip contacts the nanorod; that is, force = kx displacement. Third, the slopes of the nanorod force-displacement scans, k, decrease in scan lines recorded at increasingly large distance from the nanorod pinning point.

The Young's modulus, E, can be calculated from any single force-displacement curve using $k(x) = \frac{3\pi r^4}{4x^3}E$, where $\pi r^4/4$ is the moment of inertia for a rodlike beam of radius r. However, we have used the full set of force-displacement curves acquired as a function of position since this provides a more robust determination of E. The Young's modulus determined from a fit to the data in Figure 11 is 610 GPa.[27] In comparison, the modulus obtained from data recorded on a similar size, 10.8 nm diameter SiC nanorod was 660 GPa. These results agree well with the 600 GPa value predicted theoretically for [111] oriented SiC and the average values obtained previously for micron diameter whiskers.[29,30] Hence, we believe that our approach is a reliable one for probing the mechanics of nanobeams.

We have also used this approach to probe the mechanical properties of multishell nanotubes with diameters between 7 and 20 nm (Figure 12). In general, these data exhibit

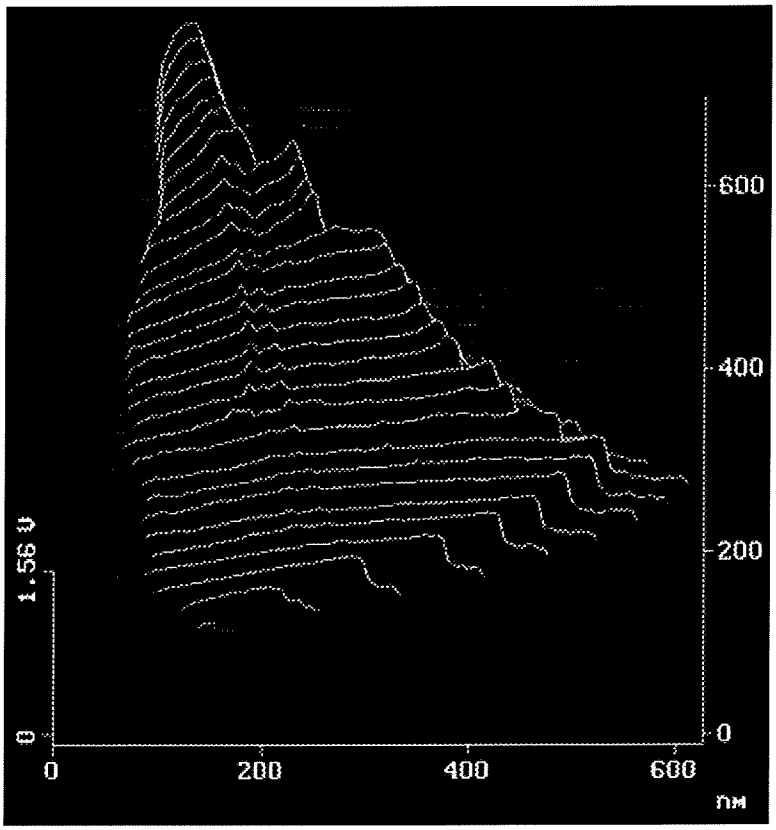

FIGURE 12

Force displacement data recorded on an 16 nm diameter carbon nanotube.

features similar to those found in the SiC nanorods experiments; that is, after contacting the nanotube during a given scan, there is an initial linear increase in the force with displacement. The nanotube data do, however, exhibit a dramatic decrease in the slope of the force-displacement curves with continued bending.[27] We believe that these measurements correspond to the first direct measure of nanotube elastic buckling that has been predicted recently in simulations.[31] Although the nanotubes exhibit a nearly two-times greater Young's modulus than SiC, 1.2 TPa, the large decrease in stiffness at the buckling points leads to an ultimate strength that is substantially less than we observe for the SiC nanorods. This has obvious implications when considering the relative merits of SiC nanorod versus carbon nanotube materials in high-strength composites.

Applications: Nanostructured Superconductors

With our emerging understanding of both synthetic methods and physical properties of 1D nanostructures, we have also begun to explore the possibility of exploiting these materials for developing nanostructured solids. A particularly exciting example of this work is the development of high critical current density (J_c), high-temperature superconductors (HTSCs).[25] Large J_cs are essential to many proposed applications of the HTSCs such as wires for power transmission cables and solenoids.[32,33] In general, J_c is limited by two major factors, including thermally activated flux motion and poor alignment of superconducting grains.[32,34,35] Thermally-activated flux flow is an intrinsic limitation and arises from the short coherence lengths and large anisotropies of the HTSC materials that lead to a weak pinning of flux-lines.[34-37] This intrinsic problem has limited the performance of $Bi_2Sr_2Ca_{n-1}Cu_nO_{2n+4}$ (BSCCO) materials at high temperatures, T, and magnetic fields, H.[38,39]

Theoretical[40,41] and experimental[42,43] studies have shown, however, that this intrinsic problem in HTSCs can be reduced significantly by creating correlated defects, such as columnar defects, in the crystal lattice. Indeed, the large enhancement of J_c produced by columnar defect structures argues that chemical (vs. physical) strategies should be considered for their creation in HTSC materials. For example, the incorporation of rodlike nanostructures into a HTSC matrix should yield the same beneficial effect as ion-generated columnar defects. There are, however, several critical constraints to achieving a useful columnar defect structure in a composite: (1) the rod-like structures must have dimensions comparable to ion damage tracks (that is, nanorods); (2) the nanorod should be chemically inert in the aggressive metal oxide environment used to prepare HTSCs; and (3) the nanorod should be oriented, not isotropically distributed, within the

superconducting matrix. From the perspective of size, carbon nanotubes are materials that might be considered for creating columnar defects, however, carbon is very reactive in the oxygen/metal oxide environments needed to prepare high-quality samples (that is, they oxidize to form CO_2 gas), and thus are not a useful approach for introducing a high-density of well-defined columnar defects.[25]

On the other hand, the MgO nanorods described above meet the above requirements for a composite. We have used these MgO nanorods to form nanostructured BSCCO composites using both the aligned nanorod forests and bulk nanorods.[25] In general, high-quality nanorod/BSCCO composites and reference BSCCO samples can be made using standard melt-texturing procedures that produce polycrystalline samples with well-oriented (textured) grains. The columnar defect structure in the nanorod/BSCCO composite is clearly seen in SEM and TEM images. TEM micrographs of composites prepared by mixing bulk MgO nanorods with prereacted BSCCO-2212 (n=2) powder and partially melting the nanorod/BSCCO pellet made from the mixture exhibit a high density of MgO nanorods in crystalline grains (Figure 13). Images recorded with the electron beam along the ***c***-axis (in-plane structure) show roughly

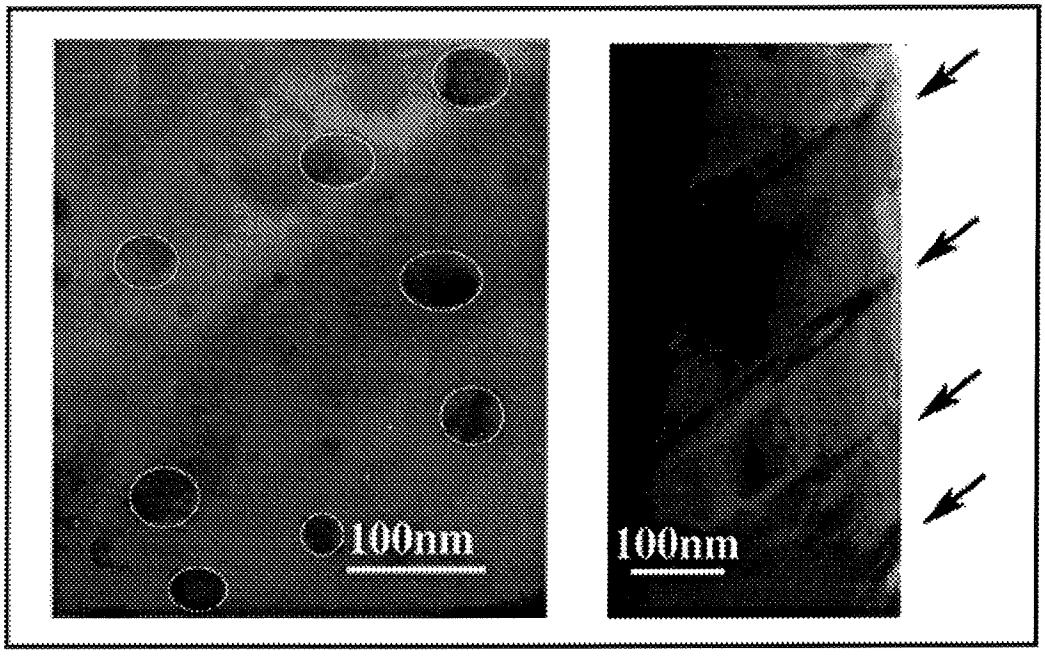

FIGURE 13

TEM image of the in-plane structure of the composite (left). Nanorods perpendicular to the copper oxide planes correspond to the darker, roughly circular spots in the image that are highlighted with white circles. The columnar nature of these defects was verified by tilting the sample off axis (right). Four MgO nanorod columnar defects are highlighted with arrows.

circular,dark spots of diameters of ~30 nm that contain primarily Mg. These features are similar to those observed on the samples containing substrate oriented nanorods (above), and thus suggest that many nanorods preferentially orient along the BSCCO ***c***-axis in these samples. The columnar structure and near ***c***-axis orientation was further confirmed by tilting and cross-sectional TEM studies of the composites.

Systematic TEM analysis of the nanorod orientation in the composites show that there are two preferred orientations: parallel and perpendicular to the ***c***-axis; that is, the nanorods are not oriented isotropically in these samples. We believe the preferred orientation or self-organization of the MgO nanorods after melt-texturing occurs because the exposed MgO surfaces are lattice-matched substrates for the growth of BSCCO with either the ***a/b*** or ***c***-axes oriented perpendicular to the nanorod axis. Hence, the synthesis of MgO nanorods serves a dual purpose: (i) this oxide minimizes deleterious reactions with the HTSC matrix and (ii) the structure leads to self-organization within BSCCO. Because oriented columnar defects are expected to produce improved J_cs compared to an isotropic distribution, we believe that the observed self-orientation of MgO nanorods during composite processing is significant for applications. More generally, our concept of self-organization, which is driven by lattice epitaxy, will be an important one to exploit in the future as we explore the synthesis of other nanostructured materials.

We have also characterized systematically J_c in the nanorod/BSCCO composites and BSCCO reference samples as a function of H and T.[25] The field-dependence of J_c determined at several temperatures for reference and composite samples is shown in Figure 14. In general, the nanorod/BSCCO composites exhibit large increases in J_c compared to the reference samples, and these increases are especially significant at higher H and T. We have shown that the large increases in J_c are due to enhanced pinning arising from nanorod columnar defects in our composite samples. There are several pieces of evidence that support this assertion. First, the increases in J_c(H,T) become more pronounced with increasing H and T. These results at elevated H and T are characteristic of the behavior expected for pinning by columnar defects, and cannot be explained by point defect pinning that characteristically shows little effect above 30 K. In addition, the enhancement in J_c exhibits an inverse dependence on the average diameter of the nanorods. These results are consistent with expectations for optimal pinning and also show the importance of developing small nanorods for the HTSC composites. Lastly, the importance of the columnar defects created by the nanorods was further checked by making composites with spherical MgO nanoclusters. While these nanocluster composites exhibited increased J_cs at low

temperature, the nanocluster composite and reference samples had comparable behavior at temperatures >25 K.

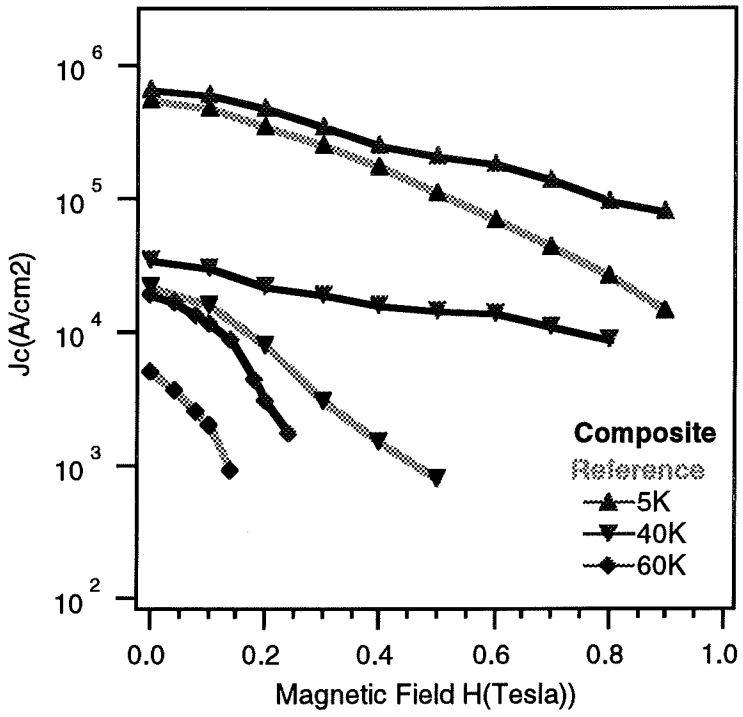

FIGURE 14

Comparison of the field dependence of J_c for BSCCO nanorod composites and BSCCO reference samples at three different temperatures.

These results compare favorably to those obtained previously in samples containing columnar defects generated by heavy-ion and proton irradiation. In general, the enhancements in J_c and shift of the irreversibility line found in the nanorod/BSCCO composites are comparable to those observed previously in ion-irradiated samples.[43-45] The maximum density of nanorod defects we have achieved, however, corresponds to an effective field of 0.25 T that is lower than achieved by ion-irradiation. Nevertheless, we believe that the ability to make samples with strong-pinning columnar defects by a rational nanochemistry approach has distinct advantages over irradiation with giga-electron volt protons for large scale applications. The development of these and other functional, nanostructured solids promises to be a central area of nanoscale chemistry in the future.

REFERENCES

1. *Nanostructures and Mesoscopic Systems*, Kirk, W. P., Reed, M. A., Eds., Academic Press, New York (1992).
2. Ashoori, R. C., *Nature* **379**, 413 (1996).
3. Alivisatos, A. P., *Science* **271**, 933 (1996).
4. Ruoff, R. S. *Nature* **372**, 731-732 (1994).
5. Guerret-Piecourt, C., Le Bouar, Y., Loiseau, A., Pascard, H., *Nature* **372**, 761-764 (1994).
6. Tsang, S. C., Chen, Y. K., Harris, P. J. F., Green, M. L. H., *Nature* **372**, 159-162 (1994).
7. Ajayan, P. M., Iijima, S. *Nature* **361**, 333-334 (1993).
8. Colbert, D. T. *et al., Science* **266**, 1218-1222 (1994).
9. Ebbesen, T. W., *Annu. Rev. Mater. Sci.* **24**, 235 (1994).
10. Iijima, S., *Nature* **354**, 56 (1991).
11. Ebbesen, T. W., Ajayan, P. M., *Nature* **358**, 220 (1992).
12. Dresselhaus, M. S., *Nature* **358**, 195 (1992).
13. Mintmire, J. W., Dunlap, B. I., White, C. T., *Phys. Rev. Lett.* **68**, 631 (1992).
14. Overney, G., Zhong, W., Tomanek, D., *Z. Phys. D* **27**, 93 (1993).
15. Dai, H., Wong, E. W., Lu, Y. Z., Fan, S., Lieber, C. M., *Nature* **375**, 769 (1995).
16. Wong, E. W., Maynor, B. W., Burns, L. D., Lieber, C. M., *Chem. Mater.* **8**, 2041 (1996).
17. Lieber, C. M., Wong, E. W., Dai, H., Maynor, B. W., Burns, L. D., *Mat. Res. Soc. Symp. Proc.* **410**, 103 (1996).
18. Wagner, R. S., Ellis, W. C., *Appl. Phys. Lett.* **4**, 89 (1964).
19. Wang, L., Wada, H., Allard, L. F., *J. Mater. Res.* **7**, 148-163 (1992).
20. Tamari, N., Kato, A., *J. Cryst. Growth* **46**, 221-237 (1979).
21. Okada, K., Nakajima, K., *Eur. Pat. Appl.*, EP 60388 A2 (1993).
22. Zhou, D., Seraphin, S., *Chem. Phys. Lett.* **222**, 233-238 (1994).
23. Morales, A. M., Lieber, C. M., *submitted for publication.*
24. Wilson, W. L., Szajowski, P. F., Brus, L. E., *Science* **262**, 1242 (1993).
25. Yang, P., Lieber, C. M., *Science* **273**, 1836 (1996).
26. Dai, H., Wong, E. W., Lieber, C. M., *Science* **272**, 523 (1996).
27. Wong, E. W., Sheehan, P. E., Lieber, C. M., *submitted for publication.*
28. Sheehan, P. E., Lieber, C. M., *Science* **272**, 1158 (1996).

29. Lambrecht, W. R. L., Segall, B., Methfessel, M., van Schilfgaarde, M., *Phys. Rev. B* **44**, 3685 (1991).
30. Petrovic, J. J., Milewski, J. V., Rohr, D. L., Gac, F. D., *J. Mater. Sci.* **20**, 1167 (1985).
31. Iijima, S., Brabec, C., Maiti, A., Bernholc, J., *J. Chem. Phys.* **104**, 2089 (1996).
32. Lubkin, G. B., *Phys. Today* **49**, 48 (1996);
33. Grant, P. M., *Nature* **375**, 107 (1995).
34. Pashitski, A. E., Polyanskii, A., Gurevich, A., Parrell, J. A., Larbalestier, D. C., *Physica C* **246**, 133 (1995).
35. Bishop, D. J., Gammel, P. L., Huse, D. A., Murray, C. A., *Science* **255,** 165 (1992).
36. Fisher, D. S., Fisher, M. P. A., Huse, D. A., *Phys. Rev. B* **43**, 130 (1991).
37. Blatter, G., Feigel'man, M. V., Geshkenbein, V. B., Larkin, A. I., Vinokur, V. M., *Rev. Mod. Phys.* **66**, 1125 (1994).
38. Li, Q., Wiesmann, H. J., Suenaga, M., Motowidlo, L., Haldar, P., *Appl. Phys. Lett.* **66**, 637 (1995).
39. Majewski, P., *Adv. Mater.* **6**, 593 (1994).
40. Nelson D. R., Vinokur, V. M., *Phys. Rev. Lett.* **68**, 2398 (1992).
41. Hwa, T., Le Doussal, P., Nelson, D. R., Vinokur, V. M., *Phys. Rev. Lett.* **71**, 3545 (1993).
42. Civale L., *et al., Phys. Rev. Lett.* **67**, 648 (1991).
43. Kummeth, P., Struller, C., Neumuller, H.-W., Saemann-Ischenko, G., *Appl. Phys. Lett.* **65**, 1302 (1994).
44. Krusin-Elbaum, L., *et al., Appl. Phys. Lett.* **64**, 3331 (1994).
45. Safar, H., *et al., Appl. Phys. Lett.* **67**, 130 (1995).